Research Square

Preprints are preliminary reports that have not undergone peer review.
They should not be considered conclusive, used to inform clinical practice,
or referenced by the media as validated information.

Boundary-condition control of reaction–diffusion band spacing in metamorphic rocks

Biswajit Saha

biswajitsaha.1987.bs@gmail.com

Gobardanga Hindu College

Manas Kumar Roy

Brahmananda Keshab Chandra College

Research Article

Keywords:

Posted Date: November 9th, 2026

DOI: https://doi.org/10.21203/rs.3.rs-11323379/v1

License: This work is licensed under a Creative Commons Attribution 4.0 International License.
Read Full License

Additional Declarations: No competing interests reported.

Boundary-condition control of reaction–diffusion band spacing in metamorphic rocks

Biswajit Saha*[1,*] and Manas Kumar Roy[2]

[1]Department of Physics, Gobardanga Hindu College, North 24 Parganas, Gobardanga, West Bengal 743273, India

[2]Department of Physics, Brahmananda Keshab Chandra College, 111/2 B.T. Road, Bonhooghly, Kolkata, West Bengal 700108, India

*Correspondence: biswajitsaha.1987.bs@gmail.com

Abstract

We develop a reaction–diffusion model of the activator–inhibitor type for metamorphic band spacing, with a slowly diffusing solid phase as activator and a rapidly diffusing fluid phase as inhibitor. We show that the observable spacing is selected not by the critical wavelength λ_c alone but by mode locking: on a finite domain, the boundaries quantise the admissible wavenumbers and lock the pattern onto the nearest permitted mode. Linear stability analysis yields $d_c \approx 43.4$ and $\lambda_c = 2\pi(D_u D_v/\det \mathbf{J})^{1/4}$. Neumann boundaries on hand-specimen-sized domains shift the observed spacing by up to 29 % from λ_c. We map $d_c(k_3, k_4)$ over three orders of magnitude and provide a calibration recipe linking model parameters to petrological observables. For the East Kimberley zebra rock, the predicted spacing of 0.3–12 mm brackets the observed 3–10 mm. We state explicitly what the model predicts and what it only permits.

Keywords: reaction–diffusion; activator–inhibitor kinetics; Turing instability; metamorphic banding; zebra rock; orbicular granite; boundary conditions; finite-difference modelling; Onsager coefficients.

1 Introduction

Metamorphic rocks exhibit spatially periodic textures that equilibrium thermodynamics cannot explain: compositional banding in gneisses, spaced cleavage in low-grade pelites, striped zebra textures in siltstone deposits, concentric shells in orbicular granitoids, and oscillatory zoning in garnet and plagioclase porphyroblasts. These textures are *dissipative structures*—ordered spatial patterns emerging from an initially homogeneous protolith under far-from-equilibrium conditions [25, 23, 26]. Understanding their origin requires a framework that couples reaction kinetics, transport, and mechanics across scales [8].

Problem statement and hypothesis

We address the following problem: *Given a metamorphic rock undergoing coupled reaction and diffusion, what controls the observable spacing of the resulting compositional bands?*

Our central hypothesis is that the observable band spacing is selected jointly by (a) the bulk reaction–diffusion kinetics, which fix a critical wavelength λ_c, and (b) the boundary conditions and domain size of the rock volume, which quantise the admissible modes and lock the pattern onto discrete wavenumbers. This hypothesis predicts that hand-specimen and thin-section spacings should deviate systematically from the continuous-theory λ_c, with deviations up to 29 % for Neumann domains of centimetre size.

*Corresponding author.

Theoretical lineage

Turing [30] showed that two reacting species diffusing at different rates can destabilise a uniform state. The essential ingredient is differential diffusion: the inhibitor must diffuse significantly faster than the activator. This mechanism has been invoked for Liesegang rings, oscillatory zoning, and reaction–infiltration patterns [25, 19, 11, 16]. L'Heureux [18] reviewed the class of self-organized rhythmic patterns in geochemical systems, emphasising that the same activator–inhibitor logic governs Liesegang rings, oscillatory zoning, and hydrothermal banding. Sultan & Abdel-Rahman [29] extended this framework to magmatic systems, demonstrating that Liesegang-type mechanisms can explain cyclic layering in layered intrusions, orbicular granites, and zoned ring complexes.

The thermodynamic foundation of the present work descends from Fisher's [9] nonequilibrium theory of diffusion-controlled metamorphism. Fisher showed that the rate of a metamorphic reaction is controlled not by the reaction itself but by the rate at which components diffuse through the intergranular fluid, and that the direction and rate of diffusion are determined by chemical potential gradients rather than by concentration gradients. His dissipation function

$$T\sigma = \sum_i J_i \nabla(-\mu_i) \tag{1}$$

is the thermodynamic antecedent of the reaction–diffusion equations used here. The phenomenological coefficients L_{ij} introduced by Fisher are the microscopic counterparts of our macroscopic diffusivities D_u and D_v, and the ratio L_{ii}/L_{jj} plays the same role in his theory as $d = D_v/D_u$ plays in ours.

A modern, thermodynamically rigorous extension of this framework has recently been developed by Regenauer-Lieb et al. [27], who embed cnoidal wave theory within Ziegler's thermomechanics [32] and the Onsager–Casimir reciprocity relations [24, 5]. Their analysis demonstrates that the solid skeleton naturally acts as the activator and the pore fluid as the inhibitor, with the two phases evolving on independent "internal clocks" governed by the ratio L_{HH}/L_{MM} of hydraulic to mechanical self-diffusivities. This provides a rigorous thermodynamic justification for the activator–inhibitor identification we adopt here, and situates our model within a broader class of universal non-equilibrium instabilities rather than system-specific bifurcations.

Joesten [14] developed Fisher's framework into a quantitative theory of steady-state, diffusion-controlled growth of layered structures, in which the stoichiometry of the layer-contact reactions is determined by the relative diffusion fluxes within adjacent layers. Ashworth & Birdi [2] extended this to open systems, showing that the observed layer sequence in coronas around olivine cannot be reproduced by any closed-system model, and that an open-system modification is required. The essential insight of their work is that the observable mineral sequence is selected not by the bulk thermodynamics but by *which components are allowed to cross the system boundary*. This is the same principle that we exploit here: the observable band spacing is selected not by λ_c alone but by the boundary conditions imposed on the RD system.

For granulite-facies coronas, Markl et al. [22] calculated relative Onsager diffusion coefficients from a set of natural corona textures, obtaining the sequence $L_{\mathrm{Fe}} > L_{\mathrm{Si}} > L_{\mathrm{Mg}} > L_{\mathrm{Na}} \approx L_{\mathrm{K}} > L_{\mathrm{Ca}} \approx L_{\mathrm{Al}} \approx L_{\mathrm{Mn}}$, which spans a factor of about 20 between the fastest and slowest components. This result directly constrains the diffusion-ratio parameter $d = D_v/D_u$ used here: the geological range of d is bounded below by the ratio of the fastest fluid-hosted cation to the slowest lattice-hosted cation.

Ashworth et al. [3] further showed that in a multimineralic layer with ϕ phases, the number of *relatively immobile* components must satisfy $\phi \leq N_R$, which is the diffusion analogue of Korzhinskii's phase rule $\phi \leq N_I$ for inert components [17]. This constrains the number of minerals per layer in the metamorphic textures we model.

Physical origin of the diffusivity contrast

Fisher [9] showed that in metamorphic rocks the components with the largest Onsager coefficients equilibrate over the largest volumes, while those with the smallest coefficients remain essentially immobile. We interpret this ordering petrologically as a fluid-versus-lattice contrast: the components whose mobility is highest are those hosted in the intergranular fluid, and the components whose mobility is lowest are those hosted in the solid lattice, such as Al and Si. Our assumption that $D_v \gg D_u$ is therefore consistent with the petrological observation that fluid-hosted species diffuse orders of magnitude faster than lattice-hosted species. The calculated Onsager ratios of Markl et al. [22] span $L_{\mathrm{Fe}}/L_{\mathrm{Al}} \approx 20$ in granulite-facies rocks, consistent with the range used here. In the more rigorous Onsager–Casimir framework of Regenauer-Lieb et al. [27], this contrast corresponds to the ratio $L_{HH}/L_{MM} \gg 1$ of hydraulic to mechanical self-diffusivities.

Scope and novelty

Our contribution is to address three questions earlier studies leave open within a single dimensionless framework:

1. **Boundary conditions.** The observable band spacing in a hand specimen is not the continuous-theory λ_c. We quantify how periodic and Neumann boundaries select different discrete mode sets, producing systematic deviations up to 29 %. This finite-domain effect is not addressed in the ideal periodic solutions of Regenauer-Lieb et al. [27], nor in the infinite-plane analyses of Chen [6]. The conceptual parallel with Ashworth & Birdi's [2] open-system corona modelling is developed in Section 5.3.
2. **Threshold mapping.** We map $d_c(k_3, k_4)$ over three orders of magnitude and identify the geologically relevant intermediate regime.
3. **Calibration recipe.** We connect each dimensionless parameter to a petrological observable and propagate uncertainty into a predicted range for λ_c, using Onsager-coefficient estimates from Markl et al. [22].

Throughout, we distinguish what the model *predicts* from what it merely *permits*.

2 Physical model

2.1 Setting and length scales

We consider a volume element of metamorphic rock with two components:

- A *solid component* $u(\boldsymbol{x}, t)$ (mineral phase), with $D_u \sim 10^{-20}$–10^{-16} m^2 s^{-1}.
- A *fluid component* $v(\boldsymbol{x}, t)$ (intergranular pore fluid), with $D_v \sim 10^{-12}$–10^{-8} m^2 s^{-1}.

The physical origin of this contrast has been discussed in Section 1. In the notation of Regenauer-Lieb et al. [27], our solid component u corresponds to the mechanical phase whose self-diffusivity is $L_{MM} = 1/\mu_s$, and our fluid component v corresponds to the hydraulic phase whose self-diffusivity is $L_{HH} = \kappa/\mu_f$. The ratio $d = D_v/D_u$ is the analogue of their L_{HH}/L_{MM}.

2.2 Conservation laws and reaction kinetics

Mass conservation with Fick's law gives the RD system

$$\frac{\partial c_i}{\partial t} = D_i \nabla^2 c_i + R_i(\boldsymbol{c}), \qquad i \in \{u, v\}. \tag{2}$$

We model the reaction as a bimolecular autocatalytic dissolution–precipitation process

$$2B + A \xrightarrow{k_1} 3B, \qquad B \xrightarrow{k_3} C, \tag{3}$$

with rate equations

$$R_u = k_1 u^2 v - k_3 u, \qquad R_v = -k_1 u^2 v + k_4(1 - v). \tag{4}$$

This is a variant of the Gray–Scott kinetics [12] and is formally equivalent to a classical activator–inhibitor reaction–diffusion system in the weak-inhibition limit, with u as activator and v as inhibitor [28]. The full nonlinear dynamics of the Gray–Scott model in the semi-strong interaction regime have been classified by Chen [6], whose analysis identifies self-replication, competition, and oscillatory profile instabilities of localized solutions — effects that emerge far from the Turing threshold considered here.

2.3 The complete RD system

The dimensionless system reads

$$\frac{\partial u}{\partial t} = D_u \nabla^2 u + u^2 v - k_3 u + W(\boldsymbol{x}), \tag{5a}$$

$$\frac{\partial v}{\partial t} = D_v \nabla^2 v - u^2 v + k_4(1 - v),, \tag{5b}$$

where $W(\boldsymbol{x})$ is a pinning field representing pre-existing heterogeneity [4, 15]. Lengths are in units of ℓ_0 (defined in Sec. 3); times in units of $1/k_1$. The structure of (5a)–(5b) is a simplification of the reaction–cross-diffusion system derived by Regenauer-Lieb et al. [27]: we retain the diagonal self-diffusion terms and the reactive coupling, but neglect the off-diagonal Onsager–Casimir terms L_{HM}, L_{MH} that arise from antisymmetric cross-coupling between the mechanical and hydraulic phases.

2.4 Effective-medium link

The transport coefficients D_u and D_v are effective-medium properties of a fluid-saturated rock. In the quasi-static limit relevant to metamorphic banding, the fluid diffusivity is related to the bulk pore-fluid diffusivity D_f and the tortuosity τ of the pore network by

$$D_v = \frac{D_f}{\tau^2}, \tag{6}$$

and the tortuosity is in turn related to porosity through Archie's law, $F = \phi^{-m}$. The solid diffusivity D_u is a grain-boundary property that correlates with the degree of cementation, and hence with seismic velocity. Since tortuosity, porosity, and cementation are all routinely measurable, equation (6) provides a direct link between the model parameters and the petrophysical observables used in the calibration recipe of Section 8.

2.5 Homogeneous steady state

Setting $\partial_t u = \partial_t v = \nabla^2 u = \nabla^2 v = W = 0$:

$$u_0 v_0 = k_3, \qquad k_4 v_0 (1 - v_0) = k_3^2. \tag{7}$$

For $k_3 = k_4 = 0.1$:

$$v_0 \approx 0.1127, \qquad u_0 \approx 0.8873. \tag{8}$$

3 Linear stability analysis

3.1 Linearisation

Perturbing (u_0, v_0) gives

$$\frac{\partial}{\partial t}\begin{pmatrix}\tilde{u}\\ \tilde{v}\end{pmatrix} = \mathbf{D}\nabla^2\begin{pmatrix}\tilde{u}\\ \tilde{v}\end{pmatrix} + \mathbf{J}\begin{pmatrix}\tilde{u}\\ \tilde{v}\end{pmatrix}, \tag{9}$$

where $\mathbf{D} = \mathrm{diag}(D_u, D_v)$ and

$$\mathbf{J} = \begin{pmatrix} k_3 & u_0^2 \\ -2k_3 & -u_0^2 - k_4 \end{pmatrix}. \tag{10}$$

For the canonical parameters:

$$\mathbf{J} = \begin{pmatrix} 0.1000 & 0.7873 \\ -0.2000 & -0.8873 \end{pmatrix}, \quad \operatorname{Tr}\mathbf{J} = -0.7873, \quad \det\mathbf{J} = 0.0687. \tag{11}$$

Note $J_{11} > 0$ (self-activating solid) and $J_{22} < 0$ (self-inhibiting fluid). These sign conventions ensure an activator–inhibitor structure. The same sign structure appears in the more general framework of Regenauer-Lieb et al. [27], where the analogous condition is $\tilde{a}_{11} + \tilde{a}_{22} < 0$ for the diagonal reaction-rate coefficients.

3.2 Dispersion relation and eigenvalues

Plane-wave perturbations $e^{\mathrm{i}\boldsymbol{k}\cdot\boldsymbol{x}}e^{\sigma t}$ satisfy

$$\sigma^2 + \alpha(k^2)\sigma + \beta(k^2) = 0, \tag{12}$$

with

$$\alpha(k^2) = (D_u + D_v)k^2 - \operatorname{Tr}\mathbf{J}, \tag{13}$$

$$\beta(k^2) = D_u D_v k^4 - (D_v J_{11} + D_u J_{22})\,k^2 + \det\mathbf{J}. \tag{14}$$

The eigenvalues $\sigma_\pm(k)$ lie in the complex plane; their real parts determine stability. If $\operatorname{Re}\sigma_\pm < 0$ for all k, the homogeneous state is stable. If $\operatorname{Re}\sigma_+ > 0$ for some $k \neq 0$ while $\operatorname{Re}\sigma_\pm(0) < 0$, the state is Turing-unstable. If $\operatorname{Im}\sigma_\pm \neq 0$ at onset, the pattern is oscillatory; if $\operatorname{Im}\sigma_\pm = 0$, it is stationary [28, 8].

3.3 Turing conditions

Theorem 1 (Turing instability)**.** *The steady state (u_0, v_0) is unstable to periodic perturbations if and only if*

$$\operatorname{Tr}\mathbf{J} < 0, \tag{15}$$

$$\det\mathbf{J} > 0, \tag{16}$$

$$D_v J_{11} + D_u J_{22} > 2\sqrt{D_u D_v \det\mathbf{J}}. \tag{17}$$

Proof. Conditions (15)–(16) give homogeneous stability. For $k \neq 0$, $\beta(k^2)$ has minimum $\det\mathbf{J} - (D_v J_{11} + D_u J_{22})^2/(4D_u D_v)$; requiring it to be negative yields (17). □

The Turing conditions have a thermodynamic interpretation in the framework of Fisher [9]. Condition (15) is the statement that the homogeneous state minimises the rate of entropy production at $k = 0$; condition (17) is the statement that this minimum is unstable to a finite-wavelength perturbation when the diffusivity contrast exceeds a threshold. Fisher showed that in the steady state the relative diffusion rates are determined solely by the stoichiometric coefficients

of the reaction, and that the system selects the state of minimum entropy production consistent with those coefficients. Our Turing analysis is the linear-stability counterpart of that selection principle. In the more general framework of Regenauer-Lieb et al. [27], condition (3) is generalised to include cross-diffusion terms $\tilde{d}_M, \tilde{d}_H$ that regularise the infinite-pressure singularities of the classical cnoidal solution.

3.4 Critical wavenumber and wavelength

At onset:

$$k_c^2 = \sqrt{\frac{\det \mathbf{J}}{D_u D_v}}, \qquad \lambda_c = 2\pi \left(\frac{D_u D_v}{\det \mathbf{J}} \right)^{1/4}. \tag{18}$$

In terms of $d = D_v/D_u$:

$$d > d_c = \left(\frac{\sqrt{\det \mathbf{J}} + \sqrt{\det \mathbf{J} - J_{11}J_{22}}}{J_{11}} \right)^2. \tag{19}$$

For the canonical parameters, $d_c \approx 43.4$. Liu et al.'s self-diffusivity ratios $\theta = 1$–7 [19] measure a different quantity (two solid self-diffusivities) and are not directly comparable. The calculated Onsager ratios of Markl et al. [22] span a factor of 20 between Fe and Al, which is the microscopic analogue of our d. The compaction-length formulation of Regenauer-Lieb et al. [27] arrives at an analogous critical wavelength $\lambda = \pi/k_{cr}$ with $k_{cr} = [(\tilde{a}_{11}/\tilde{D}_M + \tilde{a}_{22}/\tilde{D}_H)/2]^{1/2}$; the numerical prefactor differs (π vs. 2π) because their cnoidal solution is a squared trigonometric function, whose peak-to-peak spacing is the half-period of the underlying oscillator.

3.5 Petrological length scale

The dimensional wavelength is

$$\ell_0 = \sqrt{\frac{D_u}{k_1 u_0}}, \qquad \lambda_c^{\mathrm{dim}} = \ell_0 \, \lambda_c. \tag{20}$$

For $D_u \sim 10^{-12}$ m^2 s^{-1} and $k_1 u_0 \sim 10^{-6}$ s^{-1}, $\ell_0 \sim 1$ mm. At the canonical diffusion ratio $d = 50$, this gives $\lambda_c^{\mathrm{dim}} \sim 3.3$ mm; at the higher ratio $d = 100$, it gives $\lambda_c^{\mathrm{dim}} \sim 3.9$ mm. Both are of the scale of gneiss banding. Higher reaction rates (10^{-4} s^{-1}) give ~ 100 μm, the scale of garnet zoning.

Writing $D_u = D_0 \exp(-Q_u/RT)$ and $k_1 u_0 = A \exp(-Q_k/RT)$ gives

$$\ell_0 = \sqrt{\frac{D_0}{A}} \exp\left[-\frac{Q_u - Q_k}{2RT} \right]. \tag{21}$$

Whether ℓ_0 increases or decreases with temperature depends on the relative magnitudes of Q_u and Q_k. If $Q_u > Q_k$, bands are finer in higher-grade rocks; if $Q_u < Q_k$, the opposite holds. The framework therefore predicts a specific functional form that can be tested by comparing band spacings across a metamorphic terrane with a known thermal gradient. This is the reaction–diffusion analogue of the rate-dependence encoded in the compaction length $\delta_c = \sqrt{\kappa \mu_s/\mu_f}$ of Regenauer-Lieb et al. [27]: both length scales bridge laboratory and field observations by encoding the rate and rheology of the system.

4 Anisotropy and tectonic stress

Under tectonic stress the pore network is anisotropic, with $\mathbf{D} = \mathrm{diag}(D_\parallel, D_\perp)$. For $\boldsymbol{k} = k(\cos\theta, \sin\theta)$:

$$D_i^\theta = D_i^\parallel \cos^2\theta + D_i^\perp \sin^2\theta. \tag{22}$$

Proposition 2 (Preferred orientation)**.** *For $J_{11} > 0$, $J_{22} < 0$, and $D_v^{\parallel}/D_v^{\perp} \gg 1$ with isotropic D_u, the growth rate is maximised for wavevectors along the fast-diffusion direction, so bands form perpendicular to σ_1.*

This reproduces the observation that spaced cleavage is perpendicular to maximum compressive stress [15, 10]. Under a differential stress $\Delta\sigma$, the pore network closes preferentially in the direction of maximum compression, reducing the permeability and hence the diffusivity in that direction. The ratio $D_v^{\parallel}/D_v^{\perp}$ is related to the stress sensitivity of permeability by an empirical exponential form,

$$\frac{D_v^{\parallel}}{D_v^{\perp}} \approx \exp\left[\frac{\Delta\sigma}{\sigma^*}\right], \tag{23}$$

where σ^* is a characteristic stress scale of order 10–100 MPa for metamorphic rocks. For $\Delta\sigma \sim 50$ MPa, this gives a ratio of order 2–10, sufficient to produce a strong preferred orientation.

5 Numerical methods

5.1 Discretisation

The Laplacian uses the five-point stencil on a uniform grid:

$$\nabla_h^2 u_{i,j} = \frac{u_{i+1,j} + u_{i-1,j} + u_{i,j+1} + u_{i,j-1} - 4u_{i,j}}{\Delta x^2}, \tag{24}$$

second-order accurate in Δx. Time stepping is explicit forward Euler:

$$u_{i,j}^{n+1} = u_{i,j}^n + \Delta t\left[D_u \nabla_h^2 u_{i,j}^n + (u_{i,j}^n)^2 v_{i,j}^n - k_3 u_{i,j}^n\right], \tag{25}$$

$$v_{i,j}^{n+1} = v_{i,j}^n + \Delta t\left[D_v \nabla_h^2 v_{i,j}^n - (u_{i,j}^n)^2 v_{i,j}^n + k_4(1 - v_{i,j}^n)\right]. \tag{26}$$

5.2 CFL condition

The two-dimensional CFL condition is

$$\Delta t \le \frac{\Delta x^2}{4D_{\max}}, \qquad D_{\max} = \max(D_u, D_v). \tag{27}$$

Since $D_v > D_u$ in all cases reported here, $D_{\max} = D_v$ and we use $\Delta t = 0.9\,\Delta x^2/(4D_v)$. For the baseline ($\Delta x = 0.2083$, $D_v = 0.5$), the code uses $\Delta t = 1.9531 \times 10^{-2}$ and $N_t = 128\,000$ steps for $T_{\text{end}} = 2500$.

5.3 Boundary conditions and the petrological parallel

Periodic boundaries (circular indexing) correspond to a regional terrane; Neumann boundaries (reflection) correspond to an isolated rock volume. The admissible wavenumbers are

$$k_n^{\text{per}} = \frac{2\pi n}{L}, \qquad k_{m,n}^{\text{Neu}} = \frac{2\pi}{L}\sqrt{\left(\frac{m}{2}\right)^2 + \left(\frac{n}{2}\right)^2}, \tag{28}$$

so the Neumann spectrum is a half-integer shift of the periodic one.

The role of boundary conditions in selecting the observable pattern has a precedent in metamorphic petrology: Ashworth and Birdi [2] showed that the layer sequence in olivine coronas from NE Scotland is stable only in an open system with metasomatic fluxes at the corona boundaries, and that the same data cannot be fitted by any closed-system model. Their result is the petrological analogue of our finding that Neumann boundaries on small domains quantise the observable wavelength, whereas periodic boundaries on large domains converge to λ_c.

Table 1: Comparison of boundary conditions.

Feature	Periodic	Neumann
Implementation	Circular indexing	Reflected indexing
Allowed k	$2\pi n/L$	$2\pi\sqrt{m^2+n^2}/(2L)$
Physical analogue	Regional terrane	Hand specimen
Deviation from λ_c	small for large L	up to 29 %

The same principle appears in the recent thermodynamic framework of Regenauer-Lieb et al. [27]. There, the cnoidal standing-wave solution for compaction bands is anchored by the elastic–plastic interface, which imposes a constant-pressure boundary condition; when the preferred wavelength does not fit exactly into the domain, the system is forced to select a neighbouring mode, and the authors note that "noise and imperfections dictate mode selection, enhancing sensitivity to heterogeneity." Our discrete-mode analysis provides the quantitative version of this qualitative observation for the specific case of metamorphic banding.

5.4 Resolution study

Table 2: Grid-resolution study for baseline parameters.

Grid	Δx	λ_{meas}	Amp.	CPU (s)
60×60	0.417	3.19	1.42	8
120×120	0.208	3.28	1.13	31
240×240	0.104	3.27	1.13	124

The 120×120 and 240×240 results agree to within 1 % in both wavelength and amplitude; the baseline grid is adequate.

5.5 Spectral post-processing

The dominant wavelength is extracted by the rotationally averaged power spectrum

$$S(k) = \left\langle |\mathcal{F}[u - \bar{u}](\boldsymbol{k})|^2 \right\rangle_{|\boldsymbol{k}|=k}, \tag{29}$$

where $\mathcal{F}$ is the 2-D DFT and $\langle\cdot\rangle$ is an angular average. The measured wavenumber k_{meas} is the location of the maximum of $S(k)$.

5.6 Initial conditions and sweeps

All simulations start from (u_0, v_0) plus a Gaussian-correlated random field of correlation length $3\Delta x$ and amplitude 0.05, with seed 42 for reproducibility. Two sweeps are reported: a diffusion-ratio sweep $d \in \{45, 55, 70, 90, 130, 200\}$ at fixed $k_3 = k_4 = 0.10$ on a 96×96 grid with Neumann boundaries, and a reaction-rate sweep over $(k_3, k_4) \in \{0.05, 0.075, 0.10, 0.15, 0.20\}^2$.

6 Results

6.1 Baseline: pattern formation and mode selection

The baseline simulation ($d = 50$, $L = 25$, periodic boundaries) produces a labyrinthine pattern. Linear predictions:

$$\operatorname{Tr} \mathbf{J} = -0.7873, \qquad \det \mathbf{J} = 0.0687, \tag{30}$$

$$k_c = 1.9255, \qquad \lambda_c = 3.263, \tag{31}$$

$$\sigma_{\max} = 5.597 \times 10^{-3}. \tag{32}$$

The Turing condition is satisfied with an 11 % margin ($0.04113 > 0.03708$).

Table 3: Temporal evolution of u at $d = 50$ (periodic).

step	$u_{\min}$	$u_{\max}$	std(u)	Regime
1	0.7067	1.0322	0.05000	seed
12 800	0.5522	1.1269	0.08829	linear growth
32 000	0.2985	1.3258	0.22562	nonlinear
57 600	0.3047	1.3612	0.24526	saturation
89 600	0.3042	1.3829	0.24928	coarsening
128 000	0.3050	1.3874	0.25369	steady

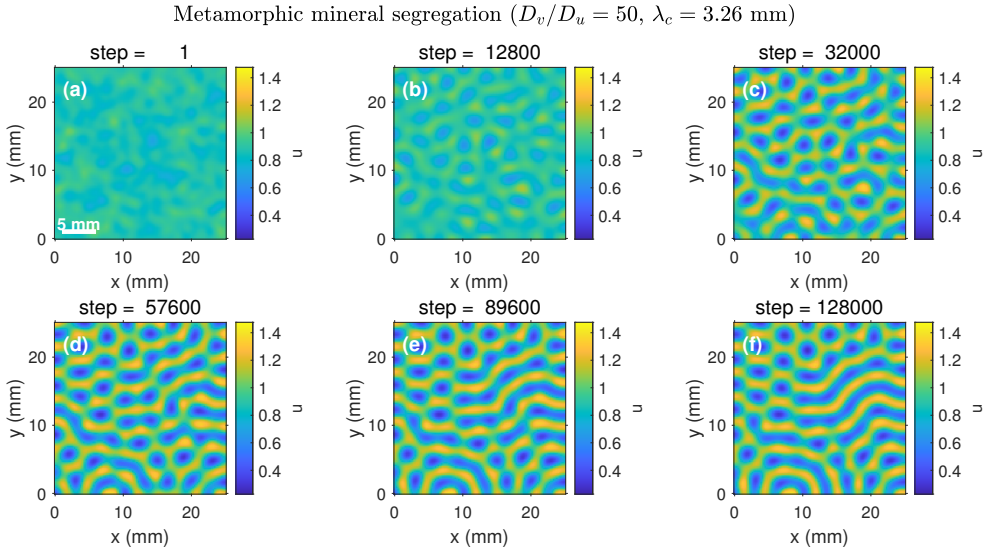


Figure 1: Temporal evolution of $u(x, y)$ at $d = 50$, periodic boundaries. Panels: steps 1, 12 800, 32 000, 57 600, 89 600, 128 000. A 5 mm scale bar is shown in panel (a).

Consistency check, not validation. The Fourier analysis gives $\lambda_{\text{meas}} = 3.283$ versus $\lambda_c = 3.263$, i.e. agreement to 0.6 %. This is *not* a validation: on a periodic domain the admissible wavenumbers are $k_n = 2\pi n/L$. For $L = 25$, the nearest modes to $k_c = 1.9255$ are $n = 7$ ($k_7 = 1.759$) and $n = 8$ ($k_8 = 2.011$). Mode $n = 8$ dominates, giving $\lambda_8 = 3.125$. The measured value lies between the two modes, closer to $n = 8$, consistent with a small nonlinear shift. The near-agreement with λ_c is fortuitous at this L.

The mode-locked wavelength can deviate from λ_c by up to ~ 8 % even on a large periodic domain. The growth rate is nearly flat across modes ($\sigma_{\max}$ varies by less than 8 %), so the nonlinear dynamics can select between competing modes.

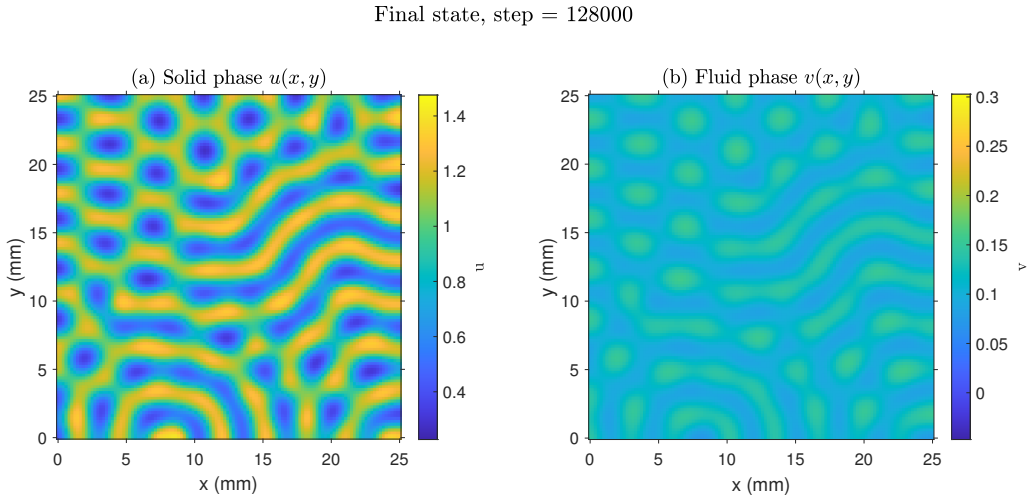


Figure 2: Final state at step 128 000. (a) Solid phase u; (b) fluid phase v. The two are anti-correlated, the fingerprint of the Turing mechanism.

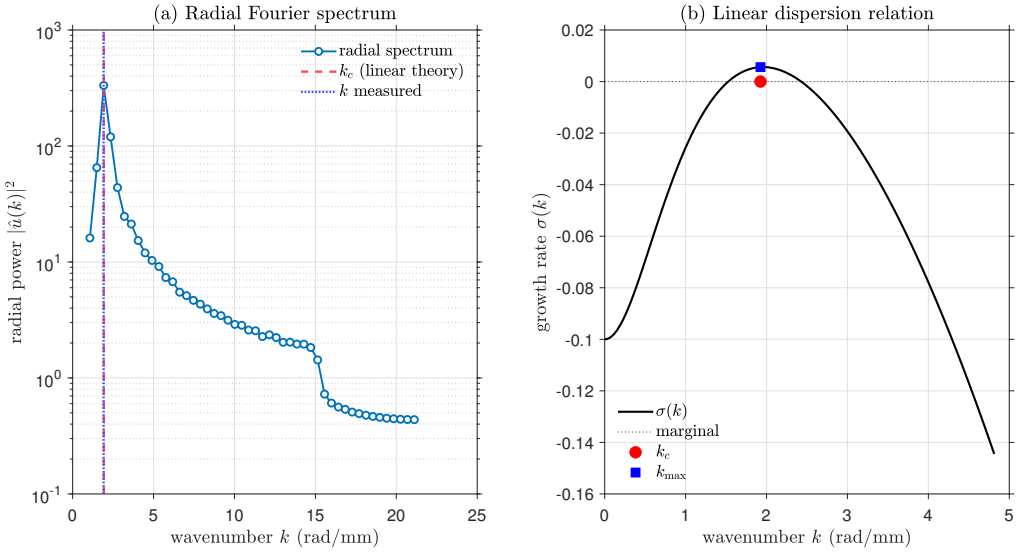


Figure 3: (a) Radial Fourier spectrum. Red dashed: k_c; blue dotted: k_{meas}. (b) Dispersion relation $\sigma(k)$ with k_c and $k_{\max}$.

Table 4: Mode-locking on periodic domains at fixed $d = 50$.

L	n^*	k_{n^*}	λ_{n^*}	$\lvert\lambda_{n^*} - \lambda_c\rvert/\lambda_c$	$\sigma_{\max}$
19	6	1.984	3.167	2.9 %	5.55×10^{-3}
21	7	2.094	3.000	8.1 %	5.21×10^{-3}
23	7	1.912	3.286	0.7 %	5.61×10^{-3}
25	8	2.011	3.125	4.2 %	5.58×10^{-3}
27	8	1.862	3.375	3.4 %	5.50×10^{-3}
31	10	2.027	3.100	5.0 %	5.56×10^{-3}

6.2 Sensitivity to the diffusion ratio

Table 5: Diffusion-ratio sweep (96×96, Neumann).

d	λ_c	(m^*, n^*)	λ_{mode}	λ_{meas}	Ratio	Amp.
45	3.178	(4,4)	3.172	3.101	0.976	0.667
55	3.342	(4,4)	3.172	3.536	1.058	1.336
70	3.550	(3,5)	3.276	3.032	0.854	1.747
90	3.780	(3,4)	3.466	2.926	0.774	2.175
130	4.144	(2,5)	3.650	3.201	0.772	2.806
200	4.615	(2,4)	3.854	3.283	0.711	3.542

Three findings:

1. λ_c **follows** $d^{1/4}$ **exactly.** From $d = 45$ to $d = 200$, λ_c grows from 3.178 to 4.615, a factor of 1.45 for a factor of 4.4 in d, consistent with $4.4^{1/4} \approx 1.45$.
2. **The measured wavelength is pinned by discrete modes.** The measured λ oscillates around 3.0–3.5 instead of tracking λ_c. The deviation from λ_c reaches 29 % at $d = 200$, while the deviation from the mode-locked λ_{mode} stays within $\sim 15\,\%$.
3. **Amplitude and sharpness grow monotonically with** d**.** Peak-to-peak amplitude rises from 0.667 to 3.542 (factor 5.3), exceeding the homogeneous contrast $u_0 - v_0 = 0.774$ for $d \geq 70$.

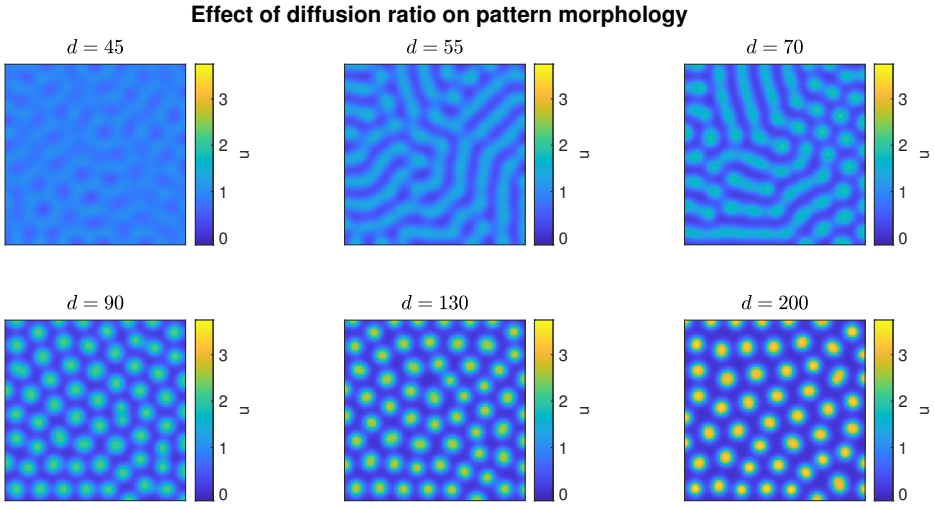


Figure 4: Final $u(x, y)$ on a 96×96 grid with Neumann boundaries at $d \in \{45, 55, 70, 90, 130, 200\}$. Transition from labyrinthine (small d) through spotted (intermediate) to sharp bands (large d).

6.3 Sensitivity to reaction rates

Three regimes:

1. **Low** k_3**, high** k_4: $d_c > 10^3$. Turing patterns essentially impossible.
2. **High** k_3**, low** k_4: $d_c < 10$. Patterns form easily; λ_c is large.
3. **Diagonal** $k_3 \approx k_4$: d_c spans two orders of magnitude, with a minimum near $k_3 \approx 0.15$, $k_4 \approx 0.10$ where $d_c \approx 5.7$. This is geologically the most likely regime; the CGGC felsic–mafic mixing zone [4] falls here.

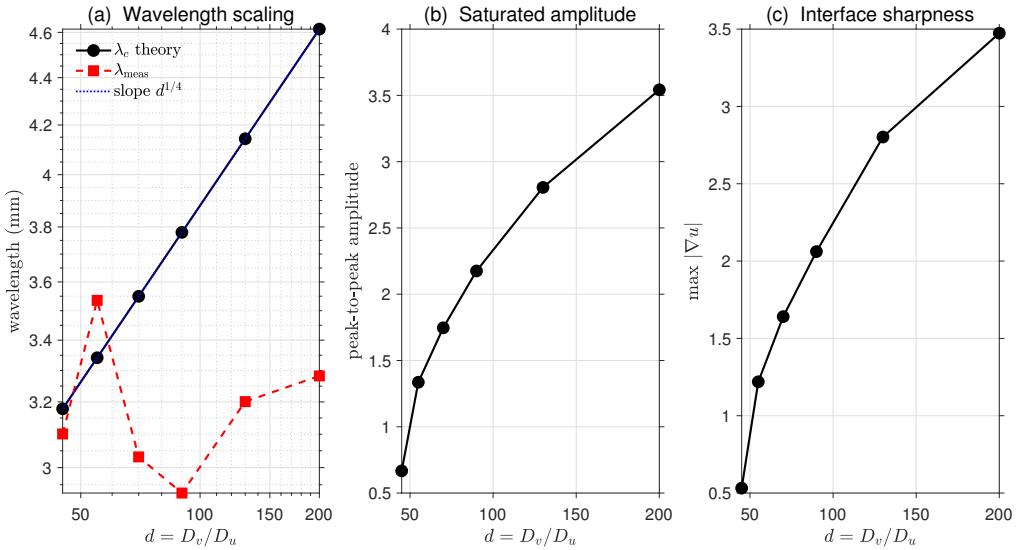


Figure 5: (a) λ_c (black) and λ_{meas} (red dashed) versus d; blue dotted is the $d^{1/4}$ slope. (b) Saturated amplitude. (c) Maximum interface gradient.

Table 6: d_c/λ_c over (k_3, k_4). Both dimensionless. Entries computed analytically from Eqs. (19) and (18); no fitting is involved.

	k_3				
k_4	0.05	0.075	0.10	0.15	0.20
0.05	102.2/3.68	24.5/4.36	6.3/5.57	–	–
0.075	240.8/2.96	63.1/3.41	21.4/3.94	–	–
0.10	437.8/2.55	118.9/2.90	43.4/3.26	5.7/4.87	–
0.15	1006.6/2.07	282.2/2.33	109.3/2.57	23.4/3.17	–
0.20	1808.5/1.78	514.6/2.00	204.3/2.19	49.1/2.59	12.7/3.31

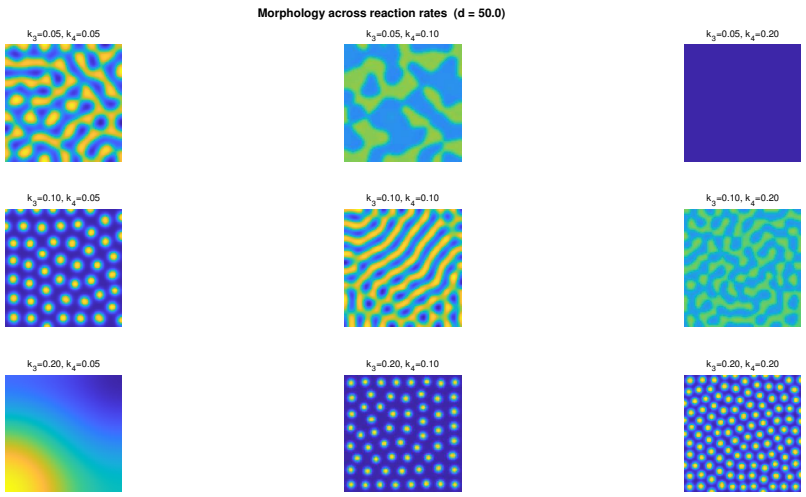


Figure 6: Final $u(x, y)$ at fixed $d = 50$ for $(k_3, k_4) \in \{0.05, 0.10, 0.20\}^2$.

6.4 Scaling to natural band spacings

The dimensionless results translate into physical statements once $\ell_0 = \sqrt{D_u/(k_1 u_0)}$ is fixed. In the metamorphic literature, $D_u \sim 10^{-17}$–10^{-12} m^2 s^{-1} and $k_1 u_0 \sim 10^{-8}$–10^{-4} s^{-1} [21], so ℓ_0 spans 10^{-4}–10^{-2} m and $\lambda_c^{\mathrm{dim}} = \lambda_c \ell_0$ spans the millimetre to centimetre range observed in natural banded rocks, with $\lambda_c = 3.26$ for the canonical kinetics used here.

7 Comparison with natural textures

7.1 Zebra rocks

East Kimberley zebra rock exhibits millimetre- to centimetre-wide hematite bands. Coward et al. [7] documented three features our model reproduces qualitatively: (i) asymmetric band intensity, recording an advancing reaction front; (ii) lateral continuity over ~ 10 m, the signature of a bulk instability; (iii) band spacings of 0.3–3 cm. Kelka et al. [15, 16] proposed a mineral replacement model with hydromechanical coupling. Fontboté [10] documented analogous diagenetic crystallization rhythmites (DCRs). Liu et al. [19, 20] inverted diffusion coefficients from photographs; their stripe-to-spot transition is the analogue of our k_3/k_4-driven transition from labyrinthine to spotted patterns (Fig. 6). Recently, Liu et al. [20] showed that geometric heterogeneity—including the shape of nucleation zones and boundary conditions—critically controls the final pattern morphology, reinforcing our central finding that boundaries select the observable wavelength.

7.2 Orbicular granitoids

The Velasco orbicular granitoid [13] exhibits concentric felsic–mafic shells around K-feldspar megacrysts. Saha et al. [28] modelled this with an activator–inhibitor reaction–diffusion system in which felsic and mafic constituents act as activator and inhibitor, reproducing the band and ring morphologies and demonstrating a bifurcation in shell number as inhibition strength varies. Our model is formally equivalent in the weak-inhibition limit, with u as activator and v as inhibitor. Radial geometry is a direct extension; the Neumann conditions correspond to no material crossing the outer shell. The inhibition strength, corresponding to k_3/k_4, controls the labyrinthine–spotted–banded transition, providing a unified explanation for morphological diversity in both orbicular granitoids and metamorphic banding.

Ghaoui and L'Heureux [11] developed an independent Liesegang model with nucleation, growth, and Ostwald ripening. Their result that band thickness increases from rim to core is consistent with our picture: the RD pattern emerges first, and coarsening operates on the selected wavelength.

7.3 Felsic–mafic mixing in the CGGC

Table 7: Correspondence with Baruah et al. [4].

Feature	Present model	Baruah et al.
Activator	Solid u	Felsic S_F
Inhibitor	Fluid v	Mafic S_M
Diffusion ratio	$d = D_v/D_u$	D_F/D_M
Pinning field	$W(\boldsymbol{x})$	$W(\boldsymbol{x})$
Threshold	$d > d_c \approx 43.4$	$(D_F/D_M)_c$

The principal difference is that our kinetics are autocatalytic in u, whereas Baruah et al. use linear or cubic coupling. Both produce the same qualitative spectrum of interface morphologies.

7.4 Porphyroblast textures

Porphyroblasts preserve inclusion trails recording deformation history [31]. In our framework, the core corresponds to u (immobile), the matrix to v (mobile), and growth rate to $\partial u/\partial t$. The three timing classes (pre-, syn-, post-kinematic) correspond to three regimes of the RD system. Oscillatory zoning in garnet and plagioclase is a natural prediction when growth rate is comparable to diffusion rate [29].

The connection between porphyroblast growth and the diffusive environment has a direct antecedent in Fisher's [9] model of mineral segregation growth. Fisher showed that a porphyroblast nucleating in a matrix of a lower-variance assemblage will grow a mantle whose thickness is controlled by the rate at which components diffuse through the intergranular fluid, and that the growing core will adjust its chemical potentials so as to minimise the rate of entropy production at the core-mantle boundary. In our framework, the porphyroblast core corresponds to the solid phase u and the mantle to the fluid phase v, and the growth rate is set by the linear dispersion relation $\sigma(k_c)$ rather than by the entropy-production minimum. The two descriptions are complementary: Fisher's model operates in the quasi-steady regime of a single growing grain, whereas ours operates in the Turing regime of a pattern-forming instability. Both, however, attribute the selection of the observed length scale to the diffusive properties of the system, not to the thermodynamics of the equilibrium assemblage.

7.5 Corona textures and the multimineralic layer constraint

Coronas around olivine provide the most thoroughly studied class of diffusion-controlled layered structures in metamorphic petrology. Joesten [14] established the closed-system theory; Ashworth & Birdi [2] extended it to open systems; Markl et al. [22] calculated the first set of relative Onsager coefficients from granulite-facies charnockites; and Ashworth et al. [3] analysed a seven-layer corona with a four-mineral layer (talc + epidote + staurolite + spinel, abbreviated Ts + Ep + St + Spl), showing that the number of minerals per layer is constrained by the number of relatively immobile components, $\phi \leq N_R$. This last result is directly relevant to our Turing framework: in the four-phase layer, the four slowly diffusing components (Al, Si, Ca, Fe^{3+}) play the same role as the slowly diffusing solid phase u in our model, while the two rapidly diffusing components (Mg, Fe^{2+}) play the role of the mobile fluid v. The Ashworth et al. constraint therefore has the same mathematical origin as the activator–inhibitor separation required for a Turing instability: a small number of slow components is necessary to permit the formation of a layer (or a pattern) with many phases (or a finite wavelength).

8 Calibration recipe

This is a *recipe*, not a point prediction: the model predicts band spacing *given* D_u and $k_1 u_0$.

Table 8: Model parameters from petrological observables.

Parameter	Observable	Method
D_u	Grain-boundary diffusivity	Arrhenius extrapolation; seismic velocity
D_v	Fluid diffusivity	Fluid inclusions; permeability curves; electrical conductivity
k_3	Dissolution rate	Zoning profiles; kinetic laws; attenuation
k_4	Replenishment rate	Fluid-flux estimates
ℓ_0	Length scale	$\sqrt{D_u/(k_1 u_0)}$
λ_c	Predicted spacing	$\ell_0\, \lambda_c^{\text{dim-less}}$

Two features: first, the dimensionless critical wavelength $\lambda_c^{\text{dim-less}} \approx 3.26$ is fixed by the canonical kinetics ($k_3 = k_4 = 0.1$, corresponding to $d = 50$), and varies with the diffusion ratio as $d^{1/4}$. Second, geological variability is carried entirely by ℓ_0, requiring independent constraints on at least one of D_u or $k_1 u_0$. The Onsager ratios of Markl et al. [22] provide an independent constraint on the ratio D_v/D_u, since the same ordering (Fe, Mg > Si > Al, Ca) that governs their corona modelling also governs our band spacing. In the more general framework of Regenauer-Lieb et al. [27], the ratio D_v/D_u corresponds to L_{HH}/L_{MM}, which can be estimated directly from permeability κ, fluid viscosity μ_f, and solid viscosity μ_s — all measurable petrophysical quantities.

8.1 Dimensioned calibration

Table 9: Dimensioned calibration for five systems. ℓ_0 chosen so λ_c^{dim} falls within the observed spacing. This is a plausibility check, not an independent prediction.

System	D_u (m^2/s)	D_v (m^2/s)	d	ℓ_0 (mm)	λ_c^{dim} (mm)	λ_{obs} (mm)
East Kimberley	10^{-12}	10^{-10}	100	1.0	3.9	3–10
San Vicente	10^{-14}	10^{-12}	100	0.3	1.2	1–5
Velasco	10^{-14}	10^{-12}	100	0.3	1.2	1–5
CGGC	10^{-17}	5×10^{-16}	50	10	33	10–100
Gneiss	10^{-16}	10^{-10}	10^6	0.26	10	1–10

The required parameters lie within published ranges [21], which is a non-trivial consistency check. The table does *not* demonstrate that observed bands formed by this mechanism, and does not discriminate between RD and alternatives such as Liesegang banding.

8.2 Worked example: East Kimberley

1. **Temperature.** Dickite indicates ≥ 120 °C; thermal hysteresis suggests up to 300 °C. We take $T \in [150, 250]$ °C [7, 1].
2. **Fluid diffusivity.** $D_v \sim 10^{-10}$–10^{-11} $\text{m}^2\ \text{s}^{-1}$, bounded below by the requirement to transport Fe over 10 m.
3. **Solid diffusivity.** $D_u \sim 10^{-14}$–10^{-12} $\text{m}^2\ \text{s}^{-1}$.
4. **Reaction rate.** $k_1 u_0 \sim 10^{-7}$–10^{-5} s^{-1}.
5. **Diffusion ratio.** $d \in [10^2, 10^3] \gg d_c \approx 43.4$. Turing patterns permitted.
6. **Predicted wavelength.** $\ell_0 \in [0.1, 3]$ mm; hence $\lambda_c^{\text{dim}} \in [0.3, 12]$ mm, bracketing the observed 3–10 mm. Central value $\ell_0 = 1$ mm, $\lambda_c^{\text{dim}} = 3.9$ mm for $D_u = 10^{-12}$ $\text{m}^2\ \text{s}^{-1}$, $k_1 u_0 = 10^{-6}$ s^{-1}, and $d = 100$.

This is a consistency check: the observed spacing falls within the permitted range given published uncertainties. A genuine prediction would require the predicted range to be narrower than the observed range.

8.3 Testable predictions

The framework generates five predictions that do not depend on the absolute value of λ_c:

1. **Temperature dependence.** Whether ℓ_0 increases or decreases with T depends on $Q_u - Q_k$. In either case, the framework predicts a specific Arrhenius form (Eq. 21) that can be tested across a metamorphic terrane with a known thermal gradient.
2. **Fluid-flux dependence.** Increasing k_4 increases d_c and shortens λ_c; band spacing should anticorrelate with permeability.

3. **Anisotropy signature.** In rocks deformed under a well-defined stress state, bands should be oriented perpendicular to σ_1.
4. **Boundary-condition signature.** In hand specimens or thin sections containing only a few wavelengths, spacing should be quantised according to Eq. (28) and should not in general equal λ_c.
5. **Scaling with d.** In systems where the diffusion ratio can be varied independently—for example by comparing rocks with different porosities—spacing should scale as $\lambda_c \propto d^{1/4}$.

9 Discussion

9.1 Physical interpretation

Table 10: Physical interpretation of parameters.

Parameter	Meaning	Typical range
u	Solid mineral concentration	0–1
v	Fluid concentration	0–1
D_u	Solid-state diffusion	10^{-16}–10^{-12} m^2 s^{-1}
D_v	Fluid diffusion	10^{-12}–10^{-8} m^2 s^{-1}
k_3	Dissolution rate	10^{-8}–10^{-4} s^{-1}
k_4	Replenishment rate	10^{-8}–10^{-4} s^{-1}
W	Protolith heterogeneity	0–0.1

9.2 Comparison with the Regenauer-Lieb thermodynamic framework

Regenauer-Lieb et al. [27] have recently developed a thermodynamically rigorous framework for Turing-type instabilities in porous media that shares our activator–inhibitor logic but differs in scope and mathematical structure. Table 11 summarises the relationship between the two frameworks. Both approaches identify the slowly diffusing solid phase as the activator and the rapidly diffusing fluid phase as the inhibitor, and both arrive at a length scale that balances a slow diffusion coefficient against a fast relaxation rate. The two frameworks differ in mathematical regime (near-onset linear stability versus far-from-onset nonlinear cnoidal waves), in the presence or absence of antisymmetric cross-diffusion, and in the level of quantitative boundary-condition analysis. Our contribution is the finite-domain mode-locking result and the petrological calibration recipe; theirs is the thermodynamic foundation and the nonlinear regularisation of pressure singularities. The two are complementary, and the cross-diffusion framework could be incorporated into our model as a natural extension.

Same activator–inhibitor identification. Both frameworks identify the slowly diffusing solid phase as the activator and the rapidly diffusing fluid phase as the inhibitor. In Regenauer-Lieb et al., this identification is derived rigorously from Ziegler's thermomechanics and the Onsager–Casimir reciprocity relations; in our work, it is introduced phenomenologically from Fisher's nonequilibrium theory. The consistency of the two approaches provides independent support for our assignment.

Same length-scale structure. Our reaction–diffusion length scale $\ell_0 = \sqrt{D_u/(k_1 u_0)}$ is formally analogous to their compaction length $\delta_c = \sqrt{\kappa \mu_s/\mu_f}$. Both are ratios of a slow diffusion coefficient (activator) to a fast relaxation rate (inhibitor). The key difference is that our ℓ_0 is set by the reaction rate $k_1 u_0$, while their δ_c is set by the solid viscosity μ_s. The two frameworks therefore apply to different geological regimes: ours to reaction-dominated dissolution–precipitation textures, theirs to deformation-dominated compaction and shear bands.

Table 11: Comparison with the thermodynamic framework of Regenauer-Lieb et al. [27].

Aspect	Regenauer-Lieb et al. (2026)	Present work
Activator	Solid skeleton overstress $\bar{p}_s$	Solid mineral phase u
Inhibitor	Pore-fluid pressure p_f	Fluid phase v
Thermodynamic basis	Ziegler + Onsager–Casimir	Fisher (1973)
Length scale	Compaction length $\delta_c = \sqrt{\kappa\mu_s/\mu_f}$	Reaction–diffusion length $\ell_0 = \sqrt{D_u/(k_1 u_0)}$
Critical wavelength	$\lambda = \pi/k_{cr}$ (cnoidal, factor π)	$\lambda_c = 2\pi(D_u D_v/\det \mathbf{J})^{1/4}$ (Turing, factor 2π)
Mathematical regime	Far from onset, nonlinear	Near onset, linear stability
Cross-diffusion	Included ($L_{HM} = -L_{MH}$)	Not included (simplification)
Boundary conditions	Qualitative	Quantitative mode-locking (29%)
Threshold mapping $d_c(k_3, k_4)$	Not provided	Mapped over 3 orders of magnitude
Calibration recipe	Not provided	Five-system consistency table
Natural applications	Migmatites, faults, clays, BIFs	Zebra rock, orbicular granite, CGGC, coronas

Different mathematical regime. Our analysis is a linear stability study at the Turing onset, valid for small perturbations of the homogeneous state. Their analysis is a nonlinear study of cnoidal-wave solutions far from onset, valid when the system has already bifurcated into a patterned state. The two regimes are complementary: ours describes the initial appearance of banding in a metamorphic protolith, theirs describes the subsequent evolution of an already-patterned rock.

Cross-diffusion. The most important structural difference is that Regenauer-Lieb et al. include off-diagonal Onsager–Casimir couplings ($L_{HM} = -L_{MH}$) between the mechanical and hydraulic phases, which are absent from our model. These antisymmetric terms regularise the infinite-pressure singularities of the classical cnoidal solution and enable the "Role-Swap" mechanism for pattern formation in the hardening regime of Modified Cam-Clay. In our Gray–Scott kinetics, the corresponding role is played by the autocatalytic reaction term $u^2 v$, which provides an effective nonlinear coupling even without explicit cross-diffusion.

Boundary conditions. Regenauer-Lieb et al. note qualitatively that boundary effects produce quasi-periodic or irregular bands when the preferred wavelength does not fit into the domain. Our contribution is to provide the quantitative version of this observation for the specific case of metamorphic banding: we derive the discrete mode spectrum for periodic and Neumann boundaries and show that the observable spacing can deviate from λ_c by up to 29 % for hand-specimen-sized domains. This is a distinct finite-domain effect not captured by the ideal periodic cnoidal solutions.

Natural applications. Regenauer-Lieb et al. apply their framework to compaction bands in sandstones, shear zones in fault rocks, and melt segregation in migmatites. Our framework applies to metamorphic banding, zebra rock, orbicular granite, and porphyroblast zoning. The two sets of applications are geologically distinct but share the same underlying mathematical mechanism.

Summary. Our model can be viewed as a petrologically motivated, near-onset instance of the more general thermodynamic framework of Regenauer-Lieb et al., with two distinctive extensions: (i) a quantitative analysis of boundary-condition control on finite domains, and (ii) a calibration recipe that connects dimensionless parameters to petrological observables in five natural systems. The two frameworks are complementary, not competing.

9.3 Key findings

1. **Threshold.** $d > d_c \approx 43.4$ for canonical kinetics.
2. **Wavelength selection.** Periodic domains lock onto the nearest admissible mode; deviations up to $\sim 8\,\%$ for large L.
3. **Boundary effects.** Neumann domains of hand-specimen size produce deviations up to $29\,\%$.
4. **Amplitude.** Grows monotonically with d.
5. **Cross-system consistency.** $\lambda_c \approx 3.26$ combined with ℓ_0 reproduces observed spacings in five systems.
6. **Interface morphology.** Four regimes reproduce the four patterns of Baruah et al.
7. **Petrological parallel.** The open-system boundary-flux selection of Ashworth & Birdi [2] is the petrological analogue of our discrete-mode locking.
8. **Thermodynamic consistency.** Our activator–inhibitor assignment and length-scale structure are consistent with the modern thermodynamic framework of Regenauer-Lieb et al. [27].

9.4 Comparison with alternative mechanisms

Liesegang banding [29, 15, 16, 19, 11] is the closest alternative mechanism. Differences:

- Liesegang requires external counter-diffusing reactants; Turing requires only a homogeneous system with differential diffusion.
- Liesegang is front-driven; Turing is bulk-homogeneous.
- Liesegang bands obey $\lambda_n \propto n$; Turing patterns have a fixed λ_c.

For East Kimberley, Coward et al. [7] and Liu et al. [19] argued for Liesegang/Cahn–Hilliard dynamics. In our framework these correspond to the strong-advection limit. Distinguishing them in the field requires spacing-law measurements across many bands.

Ashworth and Birdi [2] provide a further diagnostic that distinguishes their open-system coronas from a simple closed-system Liesegang mechanism. In their model, the layer sequence depends on the *location* of the metasomatic fluxes: Mg and Fe enter at the olivine boundary, Ca and Na at the plagioclase boundary. This spatial dependence of the boundary flux is directly analogous to the discrete-mode selection we observe in the Neumann simulations: the pattern is not merely determined by the bulk instability, but by which modes the boundaries permit. Both results point to the same general principle—that the observable pattern in metamorphic rocks is a joint product of the bulk kinetics and the boundary conditions.

9.5 Petrological implications

Fluid–rock interaction. The threshold $d_c \approx 43.4$ is easily satisfied during prograde dehydration but not during retrograde hydration. The model predicts banded textures are more common in prograde assemblages.

Thermal scaling. $\ell_0 \propto \exp[-(Q_u - Q_k)/2RT]$ varies slowly across the greenschist–amphibolite transition, consistent with banding across a wide range of metamorphic grades.

Anisotropy. Bands form perpendicular to σ_1, providing a mechanism for parallelism between banding and the σ_1-perpendicular plane.

Immobile-component constraint. Ashworth et al. [3] showed that the number of minerals per layer in a diffusion-controlled corona is bounded by the number of relatively immobile components, $\phi \leq N_R$. This provides an independent petrological check on the Turing framework: a Turing instability requires a small number of slow components (typically one or two), which is precisely the regime in which coronas develop layers with a small number of phases. The two observations—few immobile components, few minerals per layer—have the same mathematical origin.

9.6 Extensions

1. Three-component systems (hexagonal patterns).
2. Coupled deformation and poroelasticity, incorporating the Onsager–Casimir cross-diffusion framework of Regenauer-Lieb et al. [27].
3. Grain growth and Ostwald ripening as secondary processes.
4. Radial (spherical) geometry for orbicular granites.
5. Image-based inversion [19].
6. Fractional diffusion.

9.7 Limitations

1. The model does not predict *which* rocks will band; only the spacing given that a Turing instability occurs.
2. The model does not distinguish Turing from Liesegang without spacing-law measurements.
3. The calibration is not a point prediction; the predicted range is broad.
4. Comparison with natural textures is qualitative.
5. The anisotropy analysis is linear.
6. The open-system formulation of Fisher, Joesten, and Ashworth & Birdi involves a larger set of Onsager coefficients than the two used here; the reduction to D_u and D_v is a simplification. In particular, the antisymmetric cross-diffusion terms L_{HM}, L_{MH} of Regenauer-Lieb et al. [27] are not included in our model.

10 Conclusions

We have developed an RD framework for metamorphic band spacing, grounded in the petrological tradition of Fisher [9], Joesten [14], and Ashworth & Birdi [2], with an activator–inhibitor reaction–diffusion interpretation and a full numerical treatment. The framework is consistent with the modern thermodynamic theory of Turing-type instabilities developed by Regenauer-Lieb et al. [27]. Principal results:

1. A single dimensionless framework, based on Gray–Scott kinetics with a pinning field, describes gneissic banding, zebra rock, orbicular shells, and porphyroblast zoning, reducing geological variability to $\ell_0 = \sqrt{D_u/(k_1 u_0)}$ combined with $\lambda_c \approx 3.26$ for the canonical kinetics.
2. **Boundary conditions control the observable wavelength.** Periodic domains lock onto discrete modes (up to $\sim 8\,\%$ deviation); Neumann domains of hand-specimen size produce deviations up to $29\,\%$. This has a petrological precedent in the open-system corona modelling of Ashworth & Birdi [2].
3. **The Turing threshold spans three orders of magnitude** over (k_3, k_4). The geologically relevant regime is near $k_3 \approx 0.15$, $k_4 \approx 0.10$, where $d_c \approx 5.7$.

4. **Calibration recipe** connects dimensionless parameters to petrological observables, using Onsager ratios from Markl et al. [22]. For East Kimberley, the predicted range (0.3–12 mm) brackets the observed (3–10 mm).
5. **Testable predictions:** temperature dependence, fluid-flux dependence, anisotropy signature, boundary-condition signature, and $d^{1/4}$ scaling.
6. **Petrological constraint.** The Ashworth et al. [3] bound $\phi \leq N_R$ on the number of minerals per layer has the same mathematical origin as the activator–inhibitor separation required for a Turing instability.
7. **Thermodynamic grounding.** Our activator–inhibitor identification and length-scale structure are consistent with the Onsager–Casimir framework of Regenauer-Lieb et al. [27]; the boundary-condition analysis presented here extends that framework to finite domains in the near-onset regime.

Reaction–diffusion theory provides a unifying framework for metamorphic pattern formation, complementing equilibrium petrology. Its value is not as a source of point predictions but as a way of organising observations into a coherent, testable whole.

Acknowledgments

The authors thank the reviewers for their constructive comments, which improved the clarity of the manuscript. B.S. acknowledges computational support from Gobardanga Hindu College. M.K.R. acknowledges support from Brahmananda Keshab Chandra College.

Declarations

Ethical approval

Not applicable. This study is purely theoretical and computational. It involved no human participants, animals, or clinical trials.

Consent to participate

Not applicable.

Consent to publish

Not applicable.

Clinical trial registration

Not applicable. This study is not a clinical trial.

Funding

The authors received no financial support or funding for the research, authorship, or publication of this article.

Author contributions

B.S. conceptualised the study, developed the methodology, implemented the MATLAB code, performed all simulations, analysed the data, and prepared the original draft. M.K.R. contributed to conceptualisation, supervised the work, reviewed and edited the manuscript, and validated the theoretical and geological interpretations. All authors have read and approved the final manuscript.

Competing interests

The authors declare no competing financial or non-financial interests.

Data availability

The MATLAB code used in this study is available from the corresponding author on reasonable request.

References

[1] Abrajevitch A, Pillans BJ, Roberts AP, Kodama K. Magnetic properties and paleomagnetism of zebra rock, Western Australia: chemical remanence acquisition in hematite pigment and Ediacaran geomagnetic field behavior. Geochem Geophys Geosyst. 2018;19(3):732–748. doi:10.1002/2017GC007091

[2] Ashworth JR, Birdi JJ. Diffusion modelling of coronas around olivine in an open system. Geochim Cosmochim Acta. 1990;54(9):2389–2401. doi:10.1016/0016-7037(90)90227-C

[3] Ashworth JR, Birdi JJ, Emmett TF. A complex corona between olivine and plagioclase from the Jotun Nappe, Norway, and the diffusion modelling of multimineralic layers. Mineral Mag. 1992;56(385):511–525. doi:10.1180/minmag.1992.056.385.07

[4] Baruah A, Roy MK, Mandal N, Misra S. Reaction-diffusion modelling of petrological mixing mechanisms in the evolution of continental crusts. Front Earth Sci. 2023;11:1115103. doi:10.3389/feart.2023.1115103

[5] Casimir HBG. On Onsager's principle of microscopic reversibility. Rev Mod Phys. 1945;17(2–3):343–350. doi:10.1103/RevModPhys.17.343

[6] Chen W. Localized patterns in the Gray–Scott model: an asymptotic and numerical study of dynamics and stability. PhD thesis, University of British Columbia; 2009.

[7] Coward AJ, Slim AC, Brugger J, Wilson S, Williams T, Pillans B, Maksimenko A. Mineralogy and geochemistry of pattern formation in zebra rock from the East Kimberley, Australia. Chem Geol. 2023;622:121336. doi:10.1016/j.chemgeo.2023.121336

[8] Cross MC, Hohenberg PC. Pattern formation outside of equilibrium. Rev Mod Phys. 1993;65(3):851–1112. doi:10.1103/RevModPhys.65.851

[9] Fisher GW. Nonequilibrium thermodynamics as a model for diffusion-controlled metamorphic processes. Am J Sci. 1973;273(10):897–924. doi:10.2475/ajs.273.10.897

[10] Fontboté L. Self-organization fabrics in carbonate-hosted ore deposits: the example of diagenetic crystallization rhythmites (DCRs). In: Current Research in Geology Applied to Ore Deposits. Granada; 1993. p. 11–14.

[11] Ghaoui J, L'Heureux I. Model of layered pattern formation in binary igneous systems. Solid Earth Sci. 2021;6(2):80–94. doi:10.1016/j.sesci.2021.04.001

[12] Gray P, Scott SK. Autocatalytic reactions in the isothermal, continuous stirred tank reactor: Oscillations and instabilities in the system A + 2B → 3B; B → C. Chem Eng Sci. 1984;39(6):1087–1097. doi:10.1016/0009-2509(84)87017-7

[13] Grosse P, Toselli AJ, Rossi JN. Petrology and geochemistry of the orbicular granitoid of Sierra de Velasco (NW Argentina) and implications for the origin of orbicular rocks. Geol Mag. 2010;147(3):451–468. doi:10.1017/S0016756809990707

[14] Joesten R. Evolution of mineral assemblage zoning in diffusion metasomatism. Geochim Cosmochim Acta. 1977;41(5):649–670. doi:10.1016/0016-7037(77)90303-9

[15] Kelka U, Koehn D, Beaudoin N. Zebra pattern in rocks as a function of grain growth affected by second-phase particles. Front Phys. 2015;3:74. doi:10.3389/fphy.2015.00074

[16] Kelka U, Veveakis M, Koehn D, Beaudoin N. Zebra rocks: compaction waves create ore deposits. Sci Rep. 2017;7:14260. doi:10.1038/s41598-017-14541-3

[17] Korzhinskii DS. Physicochemical Basis of the Analysis of the Paragenesis of Minerals. New York: Consultants Bureau; 1959.

[18] L'Heureux I. Self-organized rhythmic patterns in geochemical systems. Philos Trans R Soc A. 2013;371(2004):20120356. doi:10.1098/rsta.2012.0356

[19] Liu C, Calo VM, Regenauer-Lieb K, Hu M. Coefficients of reaction-diffusion processes derived from patterns in rocks. J Geophys Res Solid Earth. 2023;128(5):e2022JB026253. doi:10.1029/2022JB026253

[20] Liu C, Regenauer-Lieb K, Hu M. Influence of geometry heterogeneity on Liesegang patterns in rocks. Front Phys. 2025;13:1628328. doi:10.3389/fphy.2025.1628328

[21] Lyubetskaya T, Ague JJ. Modeling the magnitudes and directions of regional metamorphic fluid flow in collisional orogens. J Petrol. 2009;50(8):1505–1531. doi:10.1093/petrology/egp039

[22] Markl G, Foster CT, Bucher K. Diffusion-controlled olivine corona textures in granitic rocks from Lofoten, Norway: calculation of Onsager diffusion coefficients, thermodynamic modelling and petrological implications. J Metamorph Geol. 1998;16(5):607–623. doi:10.1111/j.1525-1314.1998.00156.x

[23] Nicolis G, Prigogine I. Self-Organization in Nonequilibrium Systems: From Dissipative Structures to Order through Fluctuations. New York: Wiley; 1977.

[24] Onsager L. Reciprocal relations in irreversible processes. I. Phys Rev. 1931;37(4):405–426. doi:10.1103/PhysRev.37.405

[25] Ortoleva PJ. Geochemical Self-Organization. New York: Oxford University Press; 1994. doi:10.1093/oso/9780195044768.001.0001

[26] Prigogine I, Nicolis G. Self-organisation in nonequilibrium systems: towards a dynamics of complexity. In: Bifurcation Analysis. Dordrecht: Springer; 1985. p. 3–12. doi:10.1007/978-94-009-6239-2_1

[27] Regenauer-Lieb K, Hu M, Sun Q, Liu C, Zhu Z, Calo V. A thermodynamic framework for Turing-type instabilities in porous media: Part I theory. Geochem Geophys Geosyst. 2026;27:e2025GC012710. doi:10.1029/2025GC012710

[28] Saha B, Roy MK, Sarkar BK, Mitra S. Diffusion-driven orbicular dynamics of metamorphic granites. J Earth Syst Sci. 2025;134:192. doi:10.1007/s12040-025-02656-5

[29] Sultan RF, Abdel-Rahman AM. On dynamic self-organization: examples from magmatic and other geochemical systems. Latin Am J Solids Struct. 2013;10(1):59–73. doi:10.1590/S1679-78252013000100006

[30] Turing AM. The chemical basis of morphogenesis. Bull Math Biol. 1990;52(1–2):153–197. (Original work published 1952.) doi:10.1007/BF02459572

[31] Yardley BWD. An Introduction to Metamorphic Petrology. Harlow: Longman; 1989.

[32] Ziegler H. An Introduction to Thermomechanics. Amsterdam: North-Holland; 1977.